
This copy is for your personal, non-commercial use only.

If you wish to distribute this article to others, you can order high-quality copies for your colleagues, clients, or customers by [clicking here](#).

Permission to republish or repurpose articles or portions of articles can be obtained by following the guidelines [here](#).

The following resources related to this article are available online at www.sciencemag.org (this information is current as of October 29, 2014):

Updated information and services, including high-resolution figures, can be found in the online version of this article at:

<http://www.sciencemag.org/content/337/6091/204.full.html>

Supporting Online Material can be found at:

<http://www.sciencemag.org/content/suppl/2012/07/11/337.6091.204.DC1.html>

This article appears in the following **subject collections**:

Physics, Applied

http://www.sciencemag.org/cgi/collection/app_physics

were expressed during WT viral infection. However, PA-X-deficient viruses differed from the WT counterpart in their ability to cause host-cell shutoff and, moreover, caused greater clinical disease in a mouse model of IAV infection, an outcome related to an accelerated host response as assessed by microarray. PA-X is thus an accessory IAV protein that plays a consequential role at the virus-host interface. We hypothesize that defective control of host gene expression by the mutant viruses in the minority of infected lung cells provokes an altered cascade of host responses from the majority of uninfected cells. The nature of these host gene expression changes—including marked early overexpression of MHC class I genes in 1918-FS or -PTC infections, compared with 1918-WT infections—suggests that these perturbations in host response pathways affect lymphocyte activation and immune cell function that lead to an immunopathogenic inflammatory response (19). This may explain the lack of significant differences in weight loss in mice infected with 1918-WT versus 1918-FS and -PTC viruses until 5 to 8 DPI, which coincides with the appearance of influenza-specific cytotoxic T lymphocytes (25).

Taken together, these data contribute substantially to our understanding of IAV replication and pathogenesis and further suggest promising lines of inquiry into the anti-IAV immune response, as well as the factors driving IAV evolution. It is noteworthy that the outcome of infection with PA-X-null viruses was altered in the absence of differences in viral replication, as this suggests

that host immunopathology is of central importance in determining the character of disease and could therefore be a fruitful target for new therapeutics aimed at ameliorating severe IAV illness (19, 26).

References and Notes

1. P. Palese, M. L. Shaw, in *Fields Virology*, D. M. Knipe, Howley, P.M., Ed. (Lippincott Williams & Wilkins, Philadelphia, 2007), vol. 2, pp. 1647–1690.
2. J. K. Taubenberger, J. C. Kash, *Cell Host Microbe* **7**, 440 (2010).
3. K. Hara, F. I. Schmidt, M. Crow, G. G. Brownlee, *J. Virol.* **80**, 7789 (2006).
4. P. Yuan *et al.*, *Nature* **458**, 909 (2009).
5. A. Dias *et al.*, *Nature* **458**, 914 (2009).
6. J. J. Sanz-Ezquerro, S. de la Luna, J. Ortín, A. Nieto, *J. Virol.* **69**, 2420 (1995).
7. A. Rodriguez, A. Pérez-González, A. Nieto, *J. Virol.* **81**, 5315 (2007).
8. F. T. Vreede, A. Y. Chan, J. Sharps, E. Fodor, *Virology* **396**, 125 (2010).
9. E. C. Hutchinson, J. C. von Kirchbach, J. R. Gog, P. Digard, *J. Gen. Virol.* **91**, 313 (2010).
10. J. R. Gog *et al.*, *Nucleic Acids Res.* **35**, 1897 (2007).
11. A. E. Firth, N. M. Wills, R. F. Gesteland, J. F. Atkins, *Nucleic Acids Res.* **39**, 6679 (2011).
12. J. F. Atkins, R. F. Gesteland, *Recoding: Expansion of Decoding Rules Enriches Gene Expression* (Springer, Heidelberg, Germany, ed. 1, 2010).
13. J. Eisinger, B. Feuer, T. Yamane, *Nat. New Biol.* **231**, 126 (1971).
14. G. Grentzmann, J. A. Ingram, P. J. Kelly, R. F. Gesteland, J. F. Atkins, *RNA* **4**, 479 (1998).
15. J. R. Smiley, *J. Virol.* **78**, 1063 (2004).
16. F. Weber, O. Haller, *Biochimie* **89**, 836 (2007).
17. J. D. Easterbrook *et al.*, *Influenza Other Respi. Viruses* **5**, 198 (2011).
18. B. Manicassamy *et al.*, *PLoS Pathog.* **6**, e1000745 (2010).
19. J. C. Kash *et al.*, *Nature* **443**, 578 (2006).
20. H. M. Wise *et al.*, *J. Virol.* **83**, 8021 (2009).

21. W. Chen *et al.*, *Nat. Med.* **7**, 1306 (2001).
22. E. C. Holmes, D. J. Lipman, D. Zamarin, J. W. Yewdell, *Science* **313**, 1573 (2006).
23. R. Zell *et al.*, *J. Gen. Virol.* **88**, 536 (2007).
24. R. J. Garten *et al.*, *Science* **325**, 197 (2009).
25. S. A. Valkenburg *et al.*, *Microbes Infect.* **13**, 489 (2011).
26. K. B. Walsh *et al.*, *Proc. Natl. Acad. Sci. U.S.A.* **108**, 12018 (2011).

Acknowledgments: A.E.F. is supported by the Wellcome Trust (088789). P.D. was supported by the U.K. Medical Research Council (G0700815) and Wellcome Trust (073126). This work was supported in part by the intramural funds of the NIH and the National Institute of Allergy and Infectious Diseases (NIAID), NIH. J.F.A. is supported by Science Foundation Ireland (08/IN.1/B1889). K.-A.W. and A.O. were funded by Defense Threat Reduction Agency contract HDTRA-1-08-C-0023, the Luxembourg Centre for Systems Biomedicine, and the University of Luxembourg. G.L.B. and A.L. were supported by studentships from the U.K. Biotechnology and Biological Sciences Research Council and the Cambridge Infectious Disease Consortium, respectively. We thank the Comparative Medicine Branch (NIAID, NIH) for assistance with animal studies and M. Howard (Utah) for the pDluc variant of the dual luciferase vector. We also thank a number of colleagues for helpful discussion, including J. Gog and L. Tiley (University of Cambridge), W. Barclay (Imperial College London), Y. J. Tao (Rice University), J. I. Cohen, K. Subbarao, K. C. Zoon, D. C. Wilson, M. M. Gottesman, R. Wyatt, and H. Metzger (NIH). B.W.J., P.D., and J.K.T. are also thankful for the support of the NIH-Oxford-Cambridge Research Scholars program. The Gene Expression Omnibus accession no. for microarray data is GSE38112.

Supplementary Materials

www.sciencemag.org/cgi/content/full/science.1222213/DC1

Materials and Methods

Supplementary Text

Figs. S1 to S8

Table S1

References (27–33)

20 March 2012; accepted 31 May 2012

Published online 28 June 2012;

10.1126/science.1222213

REPORTS

Spin-Polarized Light-Emitting Diode Based on an Organic Bipolar Spin Valve

Tho D. Nguyen,¹ Eitan Ehrenfreund,^{1,2} Z. Valy Vardeny^{1,*}

The spin-polarized organic light-emitting diode (spin-OLED) has been a long-sought device within the field of organic spintronics. We designed, fabricated, and studied a spin-OLED with ferromagnetic electrodes that acts as a bipolar organic spin valve (OSV), based on a deuterated derivative of poly(phenylene-vinylene) with small hyperfine interaction. In the double-injection limit, the device shows ~1% spin valve magneto-electroluminescence (MEL) response, which follows the ferromagnetic electrode coercive fields and originates from the bipolar spin-polarized space charge-limited current. In stark contrast to the response properties of homopolar OSV devices, the MEL response in the double-injection device is practically independent of bias voltage, and its temperature dependence follows that of the ferromagnetic electrode magnetization. Our findings provide a pathway for organic displays controlled by external magnetic fields.

The quest for a spin-polarized organic light-emitting diode (spin-OLED) (1–3), in which the electroluminescence (EL) intensity is

sensitive to the spin polarization of the injected carriers, has been a goal in the field of organic spintronics since the successful implementation of

an organic spin valve (OSV) based on the small molecule aluminum tris(8-hydroxyquinoline) (Alq₃) (4). Despite several attempts at spin-OLEDs (1, 5) in which Alq₃ was used as the organic interlayer between two ferromagnetic (FM) electrodes in a vertical configuration, this goal has not been achieved as yet. The main obstacle in realizing such a device has been the relatively high bias voltage V_b needed for reaching substantive EL efficiency in the device at low temperatures. For example, $V_b > 10$ V is needed for EL of Alq₃ with FM electrodes at temperature $T = 10$ K, but the OSV performance sharply deteriorates with V_b and is limited to <1 V for practical operation (4, 6, 7).

We report the realization of a spin-OLED based on a bipolar OSV device that exhibits magneto-electroluminescence (MEL) on the order of ~1% at $V_b \approx 3.5$ V, with emission intensity modulation that follows the coercive fields

¹Department of Physics and Astronomy, University of Utah, Salt Lake City, UT 84112, USA. ²Physics Department and Solid State Institute, Technion-Israel Institute of Technology, Haifa 32000, Israel.

*To whom correspondence should be addressed. E-mail: val@physics.utah.edu

of the FM electrodes. Two important technical advances enabled this achievement. First, our devices are based on a deuterated organic polymer interlayer with superior spin transport properties that has a smaller hyperfine interaction than polymers based on hydrogen side groups (7). Second, we deposited a thin LiF buffer layer in front of the FM cathode to improve the electron injection efficiency (8). The bipolar OSV response has substantially different voltage, temperature, and thickness dependencies relative to the response in homopolar OSV based on the same organic interlayer. These differences are caused in part by the spin-aligned space charge-limited current (SCLC) operation upon reaching double-injection conditions during bipolar operation.

The device operation scheme (Fig. 1A) shows the injected electrons and holes initially forming polaron pairs (PPs) at the appropriate V_b needed for bipolar injection. These species are precursor excitations to singlet excitons (SEs) that may recombine radiatively and emit EL. With non-FM electrodes (Fig. 1A, panel 1), the net electron-hole bimolecular rate coefficient b for forming PPs did not depend on the magnetic field. Under the assumption of SCLC operation, the fraction of current from electron-hole recombination was inversely proportional to the rate b (9). When the OLED device was driven with FM electrodes that inject spin-aligned carriers, the rate b became field-dependent (Fig. 1A, panels 2 and 3) because the external magnetic field changed the mutual magnetization directions of the spin-injecting FM electrodes. Thus, the PP formation rate, EL intensity (MEL), and current density (magnetoconductivity, MC) all become field-dependent. This operation scenario of spin-OLED is more realistic than the simple model described in (2, 6) because the intermediate step of PP formation, as well as the spin mixing among its spin singlet (PP_s) and spin triplet (PP_t) configurations, is explicitly considered (10, 11). In fact, the spin-mixing channel is responsible for a variety of effects in OLED devices with non-FM electrodes (such as monotonic MC and MEL responses) that we term “intrinsic” MC and MEL responses (7, 11, 12), as well as EL quantum efficiency that is not limited to 25% (13).

The spin-OSV device was designed to achieve efficient EL emission at relatively low V_b (Fig. 1C), with sizable spin injection capability from the FM electrodes and with large spin diffusion length in the organic interlayer. We show the spin-OLED device structure in Fig. 1B. For the anode, we used the half-metal FM $\text{La}_{0.7}\text{Sr}_{0.3}\text{MnO}_3$ (LSMO), which has a coercive field $B_c \approx 5$ mT at cryogenic temperatures (Fig. 2D); the cathode was a FM Co thin film ($B_c \approx 35$ mT at cryogenic temperatures; Fig. 2D) capped with an Al layer for corrosion protection. The organic interlayer film, with thickness d ranging from 18 to 50 nm, was based on deuterated poly(dioctyloxy)phenyl vinylene (D-DOO-PPV), a π -conjugated polymer in which all the hydrogen atoms closest to the backbone chain were replaced by deuterium

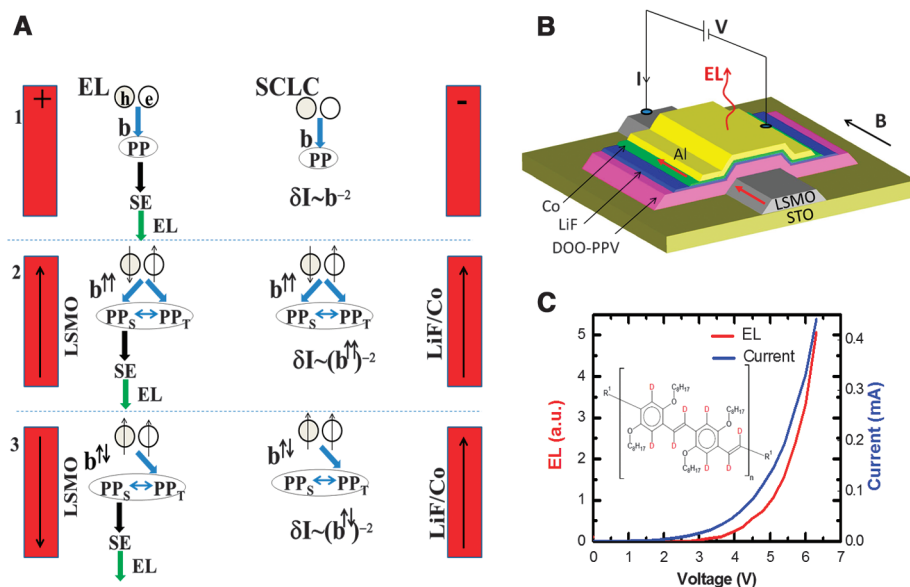


Fig. 1. (A) Spin-OLED device operation under the condition of unbalanced electron-hole space charge limited current (SCLC): (1) OLED with non-FM electrodes; the “recombination” current δI is inversely related to the efficiency of PP formation via the bimolecular recombination coefficient b ; also, $EL \propto \delta I$. (2 and 3) OLED with FM electrodes: b becomes magnetic field-dependent via the spin injection of the FM electrodes, giving rise to spin-dependent current and EL. (B) The spin-OLED device structure, where the D-DOO-PPV organic layer thickness is ~ 25 nm and LiF buffer layer thickness is ~ 1.5 nm. Here the in-plane magnetic field (black arrow) causes the FM magnetizations (red arrows) to align parallel to each other. The EL emission (wavy red line) is collected through the Co/Al thin electrode. (C) The device I - V and EL - V characteristics; the EL onset is at $V_0 \approx 3.5$ V. Inset: D-DOO-PPV polymer chemical structure.

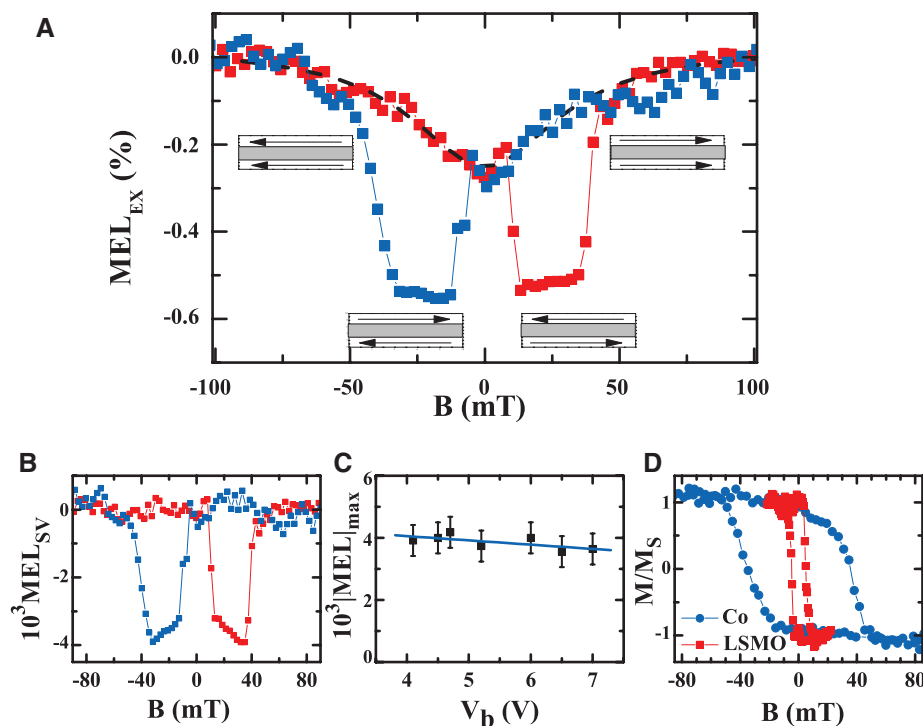


Fig. 2. Magneto-electroluminescence (MEL) response of a spin-OLED device. (A) Obtained $MEL_{EX}(B)$ response for up (red) and down (blue) B -sweeps, measured at $V_b = 4.5$ V and $T = 10$ K, for device A ($d = 25$ nm, $d' = 1.5$ nm). The black dashed line describes the nonhysteretic, intrinsic MEL background response for an up-sweep. The horizontal arrows mark the relative electrode magnetization directions. (B) The net $MEL_{SV}(B)$ response after subtraction of the background MEL from the measured MEL response shown in (A). (C) The bias voltage dependence of the maximum MEL_{SV} value. (D) Magneto-optic Kerr effect (MOKE) measurements of the LSMO and Co/LiF electrodes at 10 K that show coercive fields $B_c(\text{FM1}) \approx 5$ mT and $B_c(\text{FM2}) \approx 35$ mT, respectively.

(Fig. 1C, inset). It was previously shown (7) that the hyperfine interaction in D-DOO-PPV is considerably reduced, thus increasing the spin diffusion length λ_S to ~ 45 nm; this is about 3 times the value of λ_S in H-DOO-PPV polymer. In addition, a thin LiF layer (thickness d' ranging from 0.8 to 1.5 nm) was deposited as a buffer layer between the organic layer and Co electrode to improve electron injection (14) and to block the formation of Co inclusions (4, 15).

The turn-on voltage V_0 for sizable EL emission at the double-injection condition was reached at $V_0 \approx 3.5$ V (Fig. 1C); this value was $V_0 \approx 10$ V without the LiF layer (8). Because V_0 is still relatively high in the spin-OLED device, we conjecture that hole injection is more efficient than electron injection. This difference led to unbalanced charge injection; most of the current density was carried by the holes, whereas the EL intensity was limited by the minority electron injection from the Co/LiF cathode. Under these conditions, the “intrinsic” MEL and MC responses (7), those unrelated to the spin valve, were small (figs. S1 to S3), and this allowed us to readily study the spin valve-related MEL response.

At cryogenic temperatures, the FM LSMO (FM1) and Co (FM2) electrodes in the spin-OLED had nominal spin injection degrees of polarization of $P_1 \approx 95\%$ and $P_2 \approx 30\%$ [which may depend on the environment; see (16)]. However, P_2 substantially dropped because of the LiF buffer layer (8, 17). Because $B_c(\text{FM1}) \neq B_c(\text{FM2})$, we could switch their relative magnetization directions between parallel ($\uparrow\uparrow$) and antiparallel ($\uparrow\downarrow$) relative

alignments by sweeping the external magnetic field B (horizontal arrows in Fig. 2A), whereby the device resistance, conductance, and EL intensity depended on the relative magnetization orientations of the FM electrodes. We thus measured $\text{MEL}(B)$ and $\text{MC}(B)$ at various bias voltages, temperatures, and device thicknesses.

A typical $\text{EL}(B)$ response of a D-DOO-PPV spin-OLED measured at 10 K is plotted as $\text{MEL}_{\text{EX}}(B) \equiv [\text{EL}(B) - \text{EL}(\uparrow\uparrow)]/\text{EL}(\uparrow\uparrow)$ in Fig. 2A for a device with $d = 25$ nm and LiF $d' = 1.5$ nm. The $\text{EL}(B)$ response had two components: (i) a hysteretic negative MEL_{SV} component and (ii) a nonhysteretic positive MEL_{LSMO} component (black dashed line in Fig. 2A). The MEL_{SV} response component consisted of a downward sharp jump of $\sim 0.4\%$ in the antiparallel magnetization configuration between 4 and 30 mT that followed the electrodes' coercive fields (Fig. 2D). The MEL_{LSMO} response was caused by the magnetic properties of the LSMO electrode (4) combined with the “intrinsic” MEL response (7); it was a monotonic function of $|B|$ and symmetric with respect to $B = 0$ (fig. S2). A similar MEL component was measured before in FM-OLED devices based on Alq_3 at room temperature (1) and was ascribed to the non-spin valve MEL response of the organic interlayer. In that case, the sudden change in the $\text{EL}(B)$ response at the electrodes' respective B_c values was positive with increasing B , and was thus interpreted as having been caused by the stray field B_S that arises from the proximity of the FM electrodes to the organic interlayer. We measured B_S of the LSMO and

Co/LiF electrodes in our device (figs. S2 and S3). For devices with one FM electrode, we found $B_S(\text{LSMO}) \approx 0.7$ mT (fig. S2) and $B_S(\text{Co}) \approx 3.5$ mT (fig. S3) at cryogenic temperatures. However, the average B_S increased when two FM electrodes were deposited; in this case, we measured $B_S \approx 4$ mT (fig. S4), which is somewhat greater than in devices with one FM electrode but is too small for explaining the MEL_{SV} sharp response in our devices, given that the intrinsic MEL response is weak (fig. S1). In addition, the MEL_{SV} response was negative, in contrast to the positive MEL jump related to the stray field (I) (fig. S4).

Moreover, the MEL was isotope-dependent. We measured the MEL response in devices with different DOO-PPV isotopes (7). The spin diffusion length was isotope-dependent, and the spin valve-related MEL response indeed depended on the polymer isotope (fig. S5). Thus, the MEL response cannot be interpreted as arising from the stray fields that influence the intrinsic MEL response, as in (I). We thus conjecture that the obtained MEL_{SV} response in the bipolar OSV is a genuine spin valve effect.

To facilitate data analysis, we subtracted the nonhysteretic MEL_{LSMO} response [component (ii)] from the $\text{MEL}_{\text{EX}}(B)$ response (Fig. 2A) to obtain the “net” spin valve-related response [component (i)], $\text{MEL}_{\text{SV}}(B) \equiv \text{MEL}_{\text{EX}} - \text{MEL}_{\text{LSMO}}$ (Fig. 2B). $\text{MEL}_{\text{SV}}(B)$ displayed the typical hysteretic spin valve characteristic response with sharp jumps at the LSMO and Co coercive fields. Moreover, one of the most prominent features

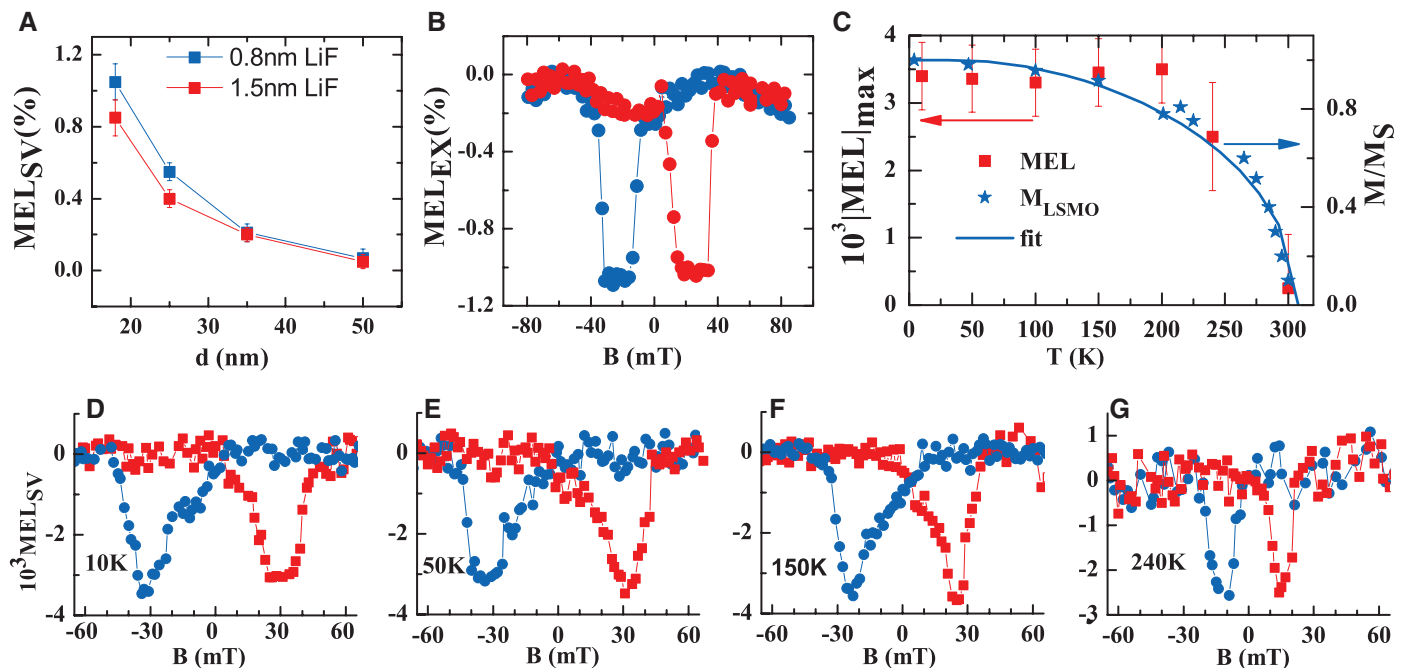


Fig. 3. (A) The maximum MEL_{SV} response of spin-OLED devices at various polymer thicknesses d and LiF buffer layer thicknesses d' of 0.8 nm (red squares) and 1.5 nm (blue squares), measured at $T = 10$ K and $V_b = 4.5$ V. (B) The optimum $\text{MEL}_{\text{SV}}(B)$ response of $\sim 1.1\%$ measured for a device with $d = 18$ nm and $d' = 0.8$ nm. (C) The maximum $\text{MEL}_{\text{SV}}(T)$ response at $V_b = 5$ V

(red squares) for a spin-OLED device with $d = 25$ nm and $d' = 1.5$ nm; the LSMO bulk magnetization versus T measured by superconducting quantum interference device (SQUID) (blue stars); and its fit using the Brillouin function $B_J(T/T_c)$ with $J = 5/2$ and $T_c = 307$ K (blue line). (D to G) $\text{MEL}(B)$ response at selected temperatures.

of the $MEL_{SV}(B)$ response is the very weak dependence of its maximum value, $MEL_{max} \equiv \max(|MEL_{SV}(B)|)$, on V_b (Fig. 2C). This response substantially differs from the strong decrease of the magnetoresistance MR_{max} with V_b in homopolar OSV devices (4, 18, 19). It is thus clear that the performance of the bipolar OSV device degrades less with V_b relative to a homopolar OSV based on the same organic layer (see below).

We measured the OSV “figure of merit” MEL_{max} at 10 K and $V = 4.5$ V for various device thicknesses d and LiF buffer layer thicknesses d' (Fig. 3A). We found that MEL_{max} decreases as d and d' increase. The decreased performance with increasing LiF d' may be readily explained as arising from the decrease of the cathode spin polarization P_2 with the LiF buffer layer thickness (8). The decreased performance with increasing organic layer d may be caused by a finite “effective” spin diffusion length λ_S at the bipolar injection condition reached here. From the device thickness dependence shown in Fig. 3A we estimate $\lambda_S \approx 25$ nm, which is different from $\lambda_S = 45$ nm obtained at small bias voltage (7). The best device performance, a MEL_{max} value of 1.1% (Fig. 3B), was obtained for a bipolar OSV device having $d = 18$ nm and $d' = 0.8$ nm (Fig. 3A). Further decreases of d and d' caused the OLED devices to become unstable.

In Fig. 3, D to G, we show $MEL_{SV}(B)$ response at various temperatures, and summarize MEL_{max} versus temperature relative to the measured LSMO bulk magnetization, $M(T)$ in Fig. 3C. The $MEL_{max}(T)$ values almost perfectly follow the

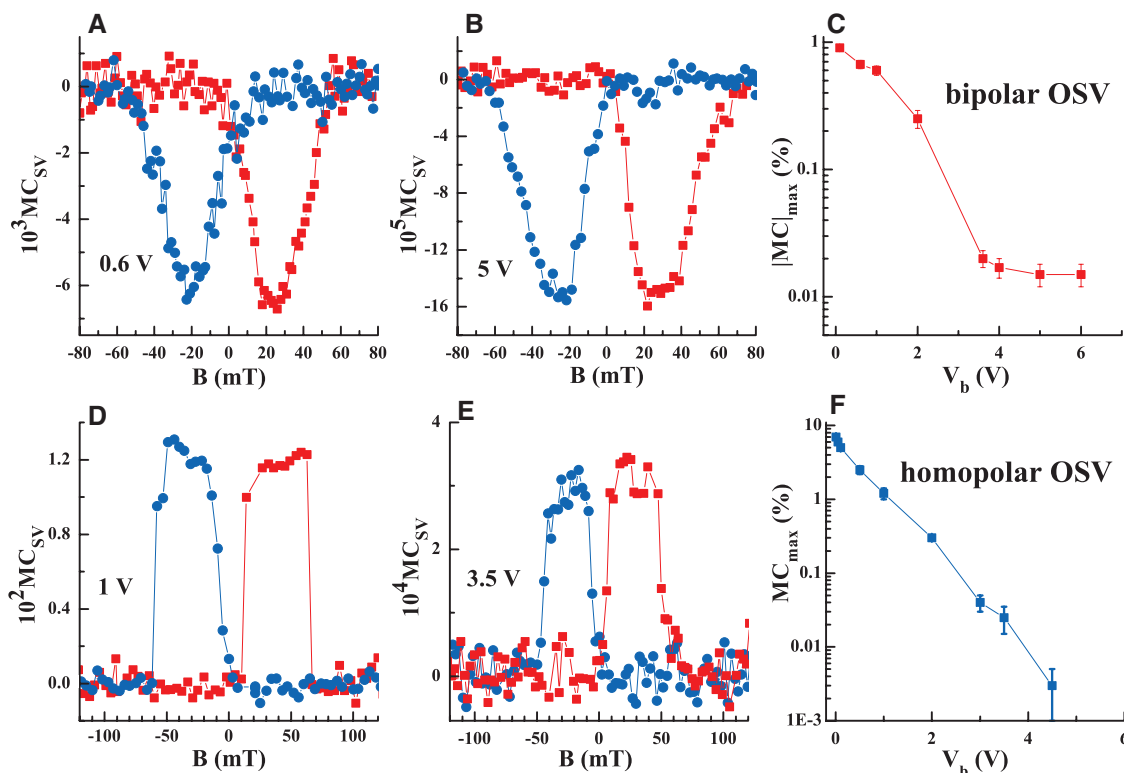
$M(T)$ response. This behavior is in stark contrast to $MR_{max}(T)$ in homopolar OSV devices, where a much steeper temperature dependence was observed (20–23) and was explained (21, 22) as having been caused by the LSMO surface magnetization decreasing with T (23).

To better compare the homopolar and bipolar OSV devices, we show in Fig. 4 the effect of the LiF buffer layer on the device magnetoconductance $MC(B)$ response. The measured response, $MC_{EX}(B) \equiv [I(B) - I(\uparrow\uparrow)]/I(\uparrow\uparrow)$, shows a nonhysteretic background that is similar to that observed in the $MEL_{EX}(B)$ response in Fig. 2A. We again subtracted this background MC response to obtain the net response $MC_{SV}(B)$, which is shown in Fig. 4, A and B, for the bipolar (LiF/Co cathode) OSV device and in Fig. 4, D and E, for the homopolar (Co cathode) OSV device. The opposite sign of the two MC response sets demonstrates that the LiF layer reverses the cathode spin polarization in agreement with (8). In Fig. 4, C and F, we show $MC_{max} \equiv \max(|MC_{SV}(B)|)$ as a function of V_b for the homopolar and bipolar OSV devices. Surprisingly, we see that although the $MC_{max}(V_b)$ dependence of the bipolar OSV device sharply decreased for $V_b < 3.5$ V, it abruptly leveled off at V_0 and became practically independent of bias voltage. This outstanding property of the bipolar OSV device facilitates the realization of spin-OLED at $V_b > V_0$.

In the following, we analyze the spin-OLED device response under conditions of unbalanced bipolar current density J where the electron current density J_e is injection-limited and $J_e \ll J$. Under these conditions, most of the device cur-

rent density is carried by the hole current J_h along with an additional small “recombination current” J_R caused by the electron-hole “recombination” that leads to PP formation (Fig. 1A). J_h , which is the sole current through the device for $V_b < V_0$, gives rise to the bias voltage-dependent MC_{SV} that is usually observed in homopolar OSV devices (7). The homopolar MC_{SV} appears to follow a Jullière-type behavior (4, 17): $MC_{SV}(V_b < V_0) \propto 2P_1P_2/(1 + P_1P_2)$, where P_1 and P_2 are the cathode and anode spin polarizations, respectively. J_R , however, turns on at $V_b \geq V_0$ and is responsible for the voltage-independent MEL_{SV} and MC_{SV} responses. These latter responses appear to follow a novel “recombination-modified” Jullière-type behavior: Both $MC_{SV}(V_b > V_0)$ and MEL_{SV} are proportional to $P_1P_2\Delta b$, where $\Delta b = b^{uu} - b^{ud}$, and b^{uu} and b^{ud} are the spin-dependent bimolecular recombination rate constants for up-up and up-down electron-hole relative spin directions, respectively. Note that although both $MC_{SV}(V_b < V_0)$ and $MC_{SV}(V_b > V_0)$ are proportional to P_1P_2 , only $MC_{SV}(V_b < V_0)$ is voltage-dependent. We thus conclude that the homopolar MC_{SV} voltage dependence cannot be caused by the FM electrode polarization as originally postulated (4), but rather originates within the device volume by a mechanism that does not affect the recombination current J_R . The electron-hole recombination products that are the singlet (PP_S) and triplet (PP_T) polaron pairs intermix through an intersystem crossing enabled via a variety of spin mixing interactions, such as the hyperfine, exchange, and spin-orbit interactions. Both same-spin polarized and opposite-spin polarized electron-hole

Fig. 4. Magnetoconductance (MC) response of bipolar and homopolar OSV devices based on D-DOO-PPV and measured at 10 K ($d = 25$ nm, $d' = 1.5$ nm). (A and B) $MC(B)$ response of bipolar OSV device measured at $V_b = 0.6$ V and 5 V, respectively, at positive (red) and negative (blue) B -sweeps. (C) Maximum MC_{SV} value versus V_b for the bipolar device. (D and E) $MC(B)$ response of homopolar OSV device measured at $V_b = 1$ V and 3.5 V, respectively, at positive (red) and negative (blue) B -sweeps. (F) Maximum MC_{SV} value versus V_b for the homopolar device.



“recombination” contribute, albeit not equally, to the steady-state PP_S density and eventually to EL (7).

To understand the obtained bipolar OSV properties, we extend the classical bipolar SCLC Parmenter-Ruppel (PR) model (9) to include FM electrodes under the condition of unbalanced current density without the effect of traps (24). In this case the J - V relation is given by

$$J = \frac{9\epsilon\epsilon_0\mu_h V^2}{8d^3} + \frac{3\mu_e\mu_h J_e}{2\mu_R^2} = J_h + J_R \quad (1)$$

where ϵ is the dielectric constant; μ_h , μ_e , and $\mu_R = \epsilon\epsilon_0 b/2e$ are the hole, electron, and recombination mobilities, respectively; b is the bimolecular recombination coefficient in the reaction rate $R_{PP} = bnp$ in which electrons of density n and holes of density p generate weakly coupled PP species (see supplementary text); J_h ($\gg J_e$) is the hole majority SCLC density; and J_R is the recombination current density. Although J_R was originally ignored by PR because $J_R \ll J_h$, here we keep this term because it is the only term that leads to EL emission.

For FM electrodes, the fraction of spin-polarized electrons injected by the cathode FM1 and collected by FM2 is $(1 \pm P_1 P_2)/2$ for $\uparrow\uparrow$ and $\uparrow\downarrow$ electrode magnetization directions, respectively, and the same is true for the fraction of spin-polarized holes that is injected by the anode FM2 and collected by FM1; here we assumed for simplicity that the spin diffusion length $\lambda_s \gg d$. In this case the spin-sensitive bimolecular recombination coefficients b^{uu} and b^{ud} cause J_R to depend on the mutual magnetization directions of the FM electrodes. The electrode magnetization-dependent SCLC can then be written as

$$J^{\uparrow\uparrow(\uparrow\downarrow)} = \frac{1}{2}(1 \pm P_1 P_2)J_h + \frac{3\mu_e\mu_h J_e}{2(\mu_R^{\uparrow\uparrow(\uparrow\downarrow)})^2} \quad (2)$$

where $\mu_R^{\uparrow\uparrow(\uparrow\downarrow)} = (\epsilon\epsilon_0 b/2e)[1 \pm P_1 P_2 \Delta b/2b]$ are the recombination mobilities for parallel and antiparallel electrode magnetizations, respectively (see supplementary text). Thus, the magnetoconductance, defined as $MC = (J^{\uparrow\uparrow} - J^{\uparrow\downarrow})/J^{\uparrow\uparrow}$ is composed of two components, MC_h , from the majority hole current, and MC_R from the recombination current. When $J_R \ll J \approx J_h$, these two components are

$$MC_h = \frac{2P_1 P_2}{1 + P_1 P_2}$$

$$MC_R = \frac{J_R}{J_h} \frac{2P_1 P_2}{[1 - (P_1 P_2 \Delta b/2b)]^2} \frac{\Delta b}{b} \quad (3)$$

where J_h and J_R are given in Eq. 1 with $\mu_R = (\mu_R^{\uparrow\uparrow} + \mu_R^{\uparrow\downarrow})/2$ and $b = (b^{uu} + b^{ud})/2$. Note that MC_h has the form of the Jullière formula (17) for a homopolar OSV, which is derived here for

the case of SCLC, whereas the new term MC_R is related to both electrode polarizations as well as the difference, Δb . For LSMO ($P_1 \approx 1$) and Co/LiF [$P_2 \approx 0.04$ at small V_b (Fig. 4F)], $(P_1 P_2)^2 \approx 10^{-3} \ll 1$ and thus $MC_h \approx 2P_1 P_2$, whereas $MC_R \approx 2P_1 P_2 (J_R/J_h)(\Delta b/b)$. We conclude that both MC_h and MC_R are proportional to $P_1 P_2$ and thus disappear in an OLED with non-FM electrodes.

The EL emission results from the radiative recombination of singlet excitons that emerge from their PP_S precursor. Thus, the EL intensity is directly proportional to the steady-state PP_S density N_{PPS} . The intermixing of $PP_S \leftrightarrow PP_T$ means that N_{PPS} is determined by both singlet and triplet channels,

$$N_{PPS}^{\uparrow\uparrow(\uparrow\downarrow)} = \frac{R_S^{\uparrow\uparrow(\uparrow\downarrow)}}{\kappa_S} + \frac{R_T^{\uparrow\uparrow(\uparrow\downarrow)}}{\kappa_T} \quad (4)$$

where

$$R_{S(T)}^{\uparrow\uparrow(\uparrow\downarrow)} \propto \frac{b^{ud(uu)} J_e}{\mu_R^{\uparrow\uparrow(\uparrow\downarrow)}} \quad (5)$$

is the singlet (triplet) channel “recombination” (or PP formation) rate, and $\kappa_{S(T)}$ designates the effective singlet (triplet) channel reaction rate, which is spin- and magnetization-independent. Using a rate equation approach to calculate N_{PPS} , we find

$$MEL = \frac{EL^{\uparrow\uparrow} - EL^{\uparrow\downarrow}}{EL^{\uparrow\uparrow}} = \frac{(\mu_R^{\uparrow\uparrow})^{-1} - (\mu_R^{\uparrow\downarrow})^{-1}}{(\mu_R^{\uparrow\uparrow})^{-1}}$$

$$= \frac{2P_1 P_2 \Delta b/2b}{1 + P_1 P_2 \Delta b/2b} \quad (6)$$

(see supplementary text). All spin-independent rates cancel out from the MEL expression. When comparing Eqs. 3 and 6, for bipolar OSV, MC and MEL have the same sign, and MEL is greater than MC by the factor J_h/J_R ($\gg 1$).

Figure 4C shows two regimes in the $MC_{SV}(V_b)$ response for the bipolar OSV. For $V_b < V_0$ (i.e., the hole-only injection regime), MC_{SV} decreases by a factor of ~ 50 between $V_b \approx 0$ and $V_b = 3.5$ V, similar to the homopolar OSV based on D-DOO-PPV (Fig. 4F). However, for $V_b > V_0$ (i.e., the bipolar injection regime), $MC_{SV}(V_b)$ is practically voltage-independent, unlike $MC_{SV}(V_b)$ of the homopolar device (Fig. 4F). Note that EL_{SV} is also voltage-independent (Fig. 2C). We thus conclude that homopolar OSV devices become less efficient at large V_b , but less so for bipolar operation. Our SCLC model separates MC_{SV} into two different components: namely, the “homopolar MC” component (MC_h in Eq. 3) and the “recombination MC” component (MC_R in Eq. 3). We conjecture that the homopolar MC component decreases with V_b , whereas the recombination MC component does not depend on V_b . For $V_b < V_0$, the bipolar MC(V_b) response is dominated by the hole-only OSV that monotonically decreases with V_b . However, as bipolar injection sets in at V_0 , the

voltage-independent MC_R takes over and the $MC(V_b)$ response becomes V_b -independent. Simultaneously, MEL is given by Eq. 6 and thus is also independent of bias voltage. MC and MEL also have the same sign for $V_b > V_0$, as predicted by Eqs. 3 and 6. In addition, the obtained ratio $MEL_{SV}/MC_{SV} \approx 25$ measured at $V_b > 4$ V (Figs. 2C and 4C) is in agreement with the larger MEL predicted by our model, where $MEL/MC \approx J_h/J_R \gg 1$.

The performance of homopolar OSV devices severely degrades with V_b (7, 16, 19). Two possible mechanisms might explain this behavior: (i) a decrease of the spin injection efficiency of the electrodes with increasing V_b via the term $P_1 P_2$, and (ii) voltage-dependent processes that occur in the organic layer. Because both MC_h and MC_R are proportional to $P_1 P_2$ (Eq. 3), but only MC_h degrades with V_b , we conjecture that the observed $MC_{SV}(V_b)$ decrease cannot originate from a decrease of $P_1 P_2$ dependence on V_b . By adding the screened Frenkel effect to the homopolar SCLC operation, the $MC_{SV}(V_b)$ decrease was recently explained as arising from the magnetic field-dependent “screening length” λ_{sc} (25). Such a mechanism would not affect the “recombination current” in a bipolar OSV for electron-hole distances $r < \lambda_{sc}$, and this may explain the voltage-independent response of the spin-OLED.

Our results provide a pathway toward organic displays controlled by external magnetic fields, but such applications would require a larger MEL and room-temperature operation. These requirements might be achieved by choosing different FM electrodes and/or organic interlayers. Finally, we note the possibility of manipulating the EL emission colors in spin-OLEDs by an external magnetic field, unlike inorganic spin-LEDs.

References and Notes

- G. Salis, S. F. Alvarado, M. Tschudy, T. Bruntschweiler, R. Allenspach, *Phys. Rev. B* **70**, 085203 (2004).
- V. A. Dediu, L. E. Hueso, I. Bergenti, C. Taliani, *Nat. Mater.* **8**, 707 (2009).
- V. Dediu, M. Murgia, F. C. Matocotta, C. Taliani, S. Barbanera, *Solid State Commun.* **122**, 181 (2002).
- Z. H. Xiong, D. Wu, Z. V. Vardeny, J. Shi, *Nature* **427**, 821 (2004).
- A. H. Davis, K. Bussmann, *J. Appl. Phys.* **93**, 7358 (2003).
- I. Bergenti *et al.*, *Org. Electron.* **5**, 309 (2004).
- T. D. Nguyen *et al.*, *Nat. Mater.* **9**, 345 (2010).
- L. Schulz *et al.*, *Nat. Mater.* **10**, 39 (2011).
- R. H. Parmenter, W. Ruppel, *J. Appl. Phys.* **30**, 1548 (1959).
- M. Yunus, P. P. Ruden, D. L. Smith, *Appl. Phys. Lett.* **93**, 123312 (2008).
- J. Kalinowski, M. Cocchi, D. Virgili, P. Di Marco, V. Fattori, *Chem. Phys. Lett.* **380**, 710 (2003).
- O. Mermer *et al.*, *Phys. Rev. B* **72**, 205202 (2005).
- M. Wohlgenannt, K. Tandon, S. Mazumdar, S. Ramasesha, Z. V. Vardeny, *Nature* **409**, 494 (2001).
- H. Ishii, K. Seki, *IEEE Trans. Electron. Dev.* **44**, 1295 (1997).
- Y. Q. Zhan *et al.*, *Appl. Phys. Lett.* **94**, 053301 (2009).
- C. Barraud *et al.*, *Nat. Phys.* **6**, 615 (2010).
- M. Jullière, *Phys. Lett. A* **54**, 225 (1975).
- H. Vinzelberg *et al.*, *J. Appl. Phys.* **103**, 093720 (2008).
- J.-W. Yoo *et al.*, *Phys. Rev. B* **80**, 205207 (2009).
- S. Majumdar, H. S. Majumdar, R. Laiho, R. Osterbacka, *J. Alloy. Comp.* **423**, 169 (2006).
- F. J. Wang, C. G. Yang, Z. V. Vardeny, X. G. Li, *Phys. Rev. B* **75**, 245324 (2007).
- V. Dediu *et al.*, *Phys. Rev. B* **78**, 115203 (2008).
- J. H. Park *et al.*, *Phys. Rev. Lett.* **81**, 1953 (1998).

24. P. N. Murgatroyd, *J. Phys. D* **3**, 151 (1970).
 25. D. Sun *et al.*, *Phys. Rev. Lett.* **104**, 236602 (2010).

Acknowledgments: Supported by NSF grant DMR-1104495 and MRSEC, DMR-1121252 program at the UoU (T.D.N. and Z.V.V.), Israel Science Foundation grant ISF 472/11 (E.E.), and Israel-USA BSF grant 2010135 (Z.V.V. and E.E.). The D-DOO-PPV

polymer synthesis was supported by U.S. Department of Energy grant DE-FG02-04ER46109. We thank X.-G. Li (USTC) for providing the LSMO substrates. The authors declare no conflict of interest associated with this work. A patent disclosure related to the spin-OLED invention was recently filed with the University of Utah, disclosure no. 5249, which has been filed as a provisional patent application.

Supplementary Materials

www.sciencemag.org/cgi/content/full/337/6091/204/DC1
 Supplementary Text
 Figs. S1 to S5

17 April 2012; accepted 31 May 2012
 10.1126/science.1223444

Dislocation-Driven Deformations in Graphene

Jamie H. Warner,^{1*} Elena Roxana Margine,¹ Masaki Mukai,² Alexander W. Robertson,¹ Feliciano Giustino,¹ Angus I. Kirkland¹

The movement of dislocations in a crystal is the key mechanism for plastic deformation in all materials. Studies of dislocations have focused on three-dimensional materials, and there is little experimental evidence regarding the dynamics of dislocations and their impact at the atomic level on the lattice structure of graphene. We studied the dynamics of dislocation pairs in graphene, recorded with single-atom sensitivity. We examined stepwise dislocation movement along the zig-zag lattice direction mediated either by a single bond rotation or through the loss of two carbon atoms. The strain fields were determined, showing how dislocations deform graphene by elongation and compression of C-C bonds, shear, and lattice rotations.

The two-dimensional (2D) structure of graphene provides unusual mechanical (1) and electronic properties (2), which can be influenced by defects and dislocations (3, 4). Defects and strain can lead to spin and magnetism in graphene that may be important for extending graphene's electronic applications to spin-based technology (5, 6). Understanding how dislocations deform graphene helps build an accurate description of both elasticity and plasticity in graphene (7–9). Studying dislocation movement (creep and climb), the interaction between dislocation pairs, and how the strain fields respond is key for developing complete structural models of graphene. So far, deep insights into dislocations in graphene have been primarily from a theoretical perspective (10–12).

Experimental investigation of dislocations in graphene at the atomic level needs high-resolution imaging, with spatial resolution sufficient to unambiguously resolve individual carbon atoms. Low-voltage transmission electron microscopy (TEM) can resolve the lattice structure of carbon-based materials such as graphitic nanomaterials and graphene (13–19) with high contrast and minimal damage. Improvement in the information limit in high-resolution TEM (HRTEM) requires the reduction of both spherical and chromatic aberration, with the latter having a notable effect at low voltages. Spherical aberration correction in HRTEM, combined with low accelerating voltage operation to reduce knock-on damage [at less than 90 kV (20)], enables

imaging of light-element atoms (including C, B, and N) in nanomaterials and molecules (14).

To image single-carbon atom dynamics in graphene using HRTEM, sufficient information transfer to unambiguously resolve the atomic positions is necessary. At low accelerating voltage, this cannot be achieved by spherical aberration correction alone and requires reducing chromatic aberration. Electron optical correction of chromatic aberration has been successfully reported (21, 22). Alternatively, the use of a monochromator to reduce the energy spread in the incident electron beam provides a way of limiting chromatic effects (23). There have been several reports of HRTEM imaging of graphene both with (24) and without (25, 26) monochromation at an accelerating voltage of 80 kV, but only relatively small differences in the resolution of images have been demonstrated. Indirect exit-wave reconstruction has also been used to characterize a fully resolved atomic structure for a monolayer/bilayer interface (27). However, this technique requires numerous images to generate the complex exit wave and is thus not suitable for the investigation of real-time single-atom dynamics, which are essential for monitoring structural transformations.

In this paper, we present low-voltage HRTEM imaging of dislocation dynamics in graphene, using both spherical aberration correction and monochromation of the electron beam using a double Wien filter (figs. S1 to S4). Graphene samples were prepared using chemical vapor deposition (CVD) on copper foils (28) and were transferred onto silicon nitride TEM grids with 2- μm holes (see the supplementary materials for details) (29).

Figure 1A shows a single HRTEM image of monolayer graphene containing a pair of edge

dislocations aligned in opposite directions with (1,0) form, consisting of a pentagon-heptagon pair (10). Previous work has suggested the presence of a single dislocation in graphene (19) and a pair of dislocations in reduced graphene oxide (30), but the image resolution in those studies was not sufficient to resolve the individual atomic positions required to determine the exact structure. Figure 1B shows an atomic model, and Fig. 1C shows the multislice HRTEM image simulation for the dislocation pair observed in Fig. 1A.

There are five possible mechanisms that describe how these dislocation pairs could have formed: during the CVD growth, electron beam sputtering of carbon dimers along a zig-zag lattice direction, from surface adatom incorporation, from a mono vacancy, or from a Stone-Wales defect (figs. S5 to S7). Initial observation of the area of the sample in Fig. 1 showed that it was free from dislocations and monovacancies (fig. S8), which indicates that the dislocations were

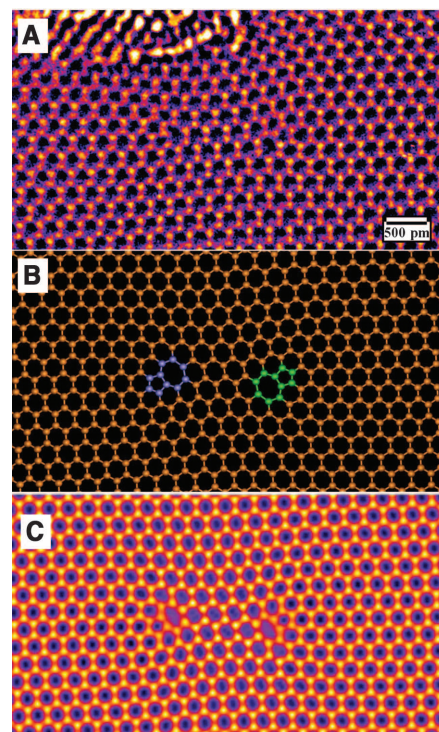


Fig. 1. Imaging edge dislocations. (A) HRTEM image showing two opposing (1,0) edge glide dislocations in graphene. (B) Structural model representing the dislocation pair (blue and green) in (A). (C) HRTEM image simulations using the atomic model in (B) as a supercell. False color is used for the images to aid visual inspection.

¹Department of Materials, University of Oxford, Parks Road, Oxford OX1 3PH, UK. ²JEOL, 3-1-2 Musashino, Akishima, Tokyo 196-8558, Japan.

*To whom correspondence should be addressed. E-mail: jamie.warner@materials.ox.ac.uk